Multiobjective crashworthiness optimization design of functionally graded foam-filled tapered tube based on dynamic ensemble metamodel

Article *in* Materials & Design (1980-2015) · October 2013

CITATIONS
69

READS
308

7 authors, including:

Hanfeng Yin
Hunan University
59 PUBLICATIONS **2,036** CITATIONS
SEE PROFILE

Guilin Wen
Hunan University
183 PUBLICATIONS **4,458** CITATIONS
SEE PROFILE

Materials and Design 55 (2014) 747–757

Contents lists available at ScienceDirect

Materials and Design

journal homepage: www.elsevier.com/locate/matdes

Multiobjective crashworthiness optimization design of functionally graded foam-filled tapered tube based on dynamic ensemble metamodel

Hanfeng Yin [a,b], Guilin Wen [a,b,*], Hongbing Fang [c], Qixiang Qing [b], Xiangzheng Kong [b], Jiuru Xiao [b], Zhibo Liu [b]

[a] State Key Laboratory of Advanced Design and Manufacturing for Vehicle Body, Hunan University, Changsha, Hunan 410082, PR China
[b] Key Laboratory of Advanced Design and Simulation Techniques for Special Equipment, Ministry of Education, Hunan University, Changsha, Hunan 410082, PR China
[c] Department of Mechanical Engineering and Engineering Science, The University of North Carolina at Charlotte, Charlotte, NC 28223-0001, USA

ARTICLE INFO

Article history:
Received 30 June 2013
Accepted 19 October 2013
Available online 30 October 2013

Keywords:
Crashworthiness
Multiobjective optimization
Functionally graded foam
Foam-filled tube
Metamodel

ABSTRACT

Foam-filled thin-walled structures have recently gained attention with increasing interest due to their excellent energy absorption capacity. In this study, a new type of foam-filled thin-walled structure called as functionally graded foam-filled tapered tube (FGFTT) is proposed. FGFTT consists of graded density foam and thin-walled tapered tube. In order to investigate the energy absorption characteristics of FGFTTs, the numerical simulations for two kinds of FGFTTs subjected to axial dynamical loading are carried out by nonlinear finite element code LS-DYNA. In addition, a new kind of multiobjective crashworthiness optimization method employing the dynamic ensemble metamodeling method together with the multiobjective particle swarm optimization (MOPSO) algorithm is presented. This new kind of multiobjective crashworthiness optimization method is then used to implement the crashworthiness optimization design of FGFTTs. Meanwhile, the crashworthiness optimization designs of FGFTTs are implemented by using traditional multiobjective crashworthiness optimization method, which employs metamodels such as polynomial response surface (PRS), radial basis function (RBF), kriging (KRG), support vector regression (SVR) or the ensemble with the static design of experiment (DOE). Finally, by comparing the optimal designs of FGFTTs obtained by using the new multiobjective crashworthiness optimization method and the traditional one, the results show that the proposed new crashworthiness optimization method is more feasible.

1. Introduction

Foam-filled thin-walled structure has been widely used in impact engineering such as vehicle crashworthiness for its excellent energy absorption and extraordinary light weight [1]. Thus, a lot of work on studying the energy absorption characteristics of foam-filled thin-walled structures by employing experimental, analytical and numerical methods [2–18] has been extensively investigated. According to the results reported, it can be found that foam-filled thin-walled structures can absorb more dynamic impact energy than the corresponding hollow thin-walled structures. The energy absorption of a foam-filled thin-walled structure is larger than the sum of the energy absorptions of individual filled foam and thin-walled structure. The improvement is due to an interaction between the foam and the thin wall. Among those different kinds of foam-filled thin-walled structures, the foam-filled tapered thin-walled structure has been gradually become a very attractive and newborn subject because it not only has excellent energy absorption capacity but also performs superior balance of crashing stability [19,20].

However, the investigations on foam-filled thin-walled structures in the existing literature mainly focus on the uniform density foams. Recently, for some popular foam-filled thin-walled structures, the functionally graded foam (FGF) material is considered to replace the uniform foam (UF) material. For instance, Sun et al. [21] studied the energy absorption characteristics of FGF-filled square tubes in comparison with the UF-filled square tubes. It is found that the crashworthiness of FGF-filled tube is better than that of the corresponding UF-filled tube. In their work, the density of the filled foams of FGF-filled tubes changes along the axial direction of the tube. Yin et al. [22] investigated the energy absorption characteristics of two kinds of functionally lateral graded foam (FLGF) filled square tubes. The investigation results show that FLGF-filled square tube has better energy absorption than UF-filled square tube with the same weight. Attia et al. [23] employed nonlinear finite element code LS-DYNA to

* Corresponding author at: State Key Laboratory of Advanced Design and Manufacturing for Vehicle Body, Hunan University, Changsha, Hunan 410082, PR China. Tel.: +86 731 88821482; fax: +86 731 88822051.
E-mail address: glwen@hnu.edu.cn (G. Wen).

0261-3069/$ - see front matter © 2013 Elsevier Ltd. All rights reserved.
http://dx.doi.org/10.1016/j.matdes.2013.10.054

investigate the crashworthiness of the FGF-filled square tubes, in which the foam density changes along both the axial and lateral directions of the tubes. The numerical results show relative improvement of 12% in specific energy absorption levels of FGF-filled structures over their uniform density counterparts with the same mass. Based on the above investigations, it can be found that the crashworthiness of FGF-filled thin-walled structures is usually better than that of their uniform density counterparts. FGF-filled tapered thin-walled structures are likely to be a good alternative energy absorber in vehicle engineering, because UF-filled tapered thin-walled structure performs better crashing stability. However, to our best knowledge, the FGF-filled tapered thin-walled structures had never been presented or investigated before.

Note that for both UF-filled structures and FGF-filled structures, the crashworthiness of foam-filled thin-walled structures is greatly affected by the design parameters such as structural size and foams density. In order to optimize the crashworthiness of foam-filled thin-walled structures, it is essential to develop some design methods to seek for the optimal parameters, see the references in [24–29]. It should be mentioned that some metamodels of optimal objectives were usually used in optimization design processes to reduce the computational cost. The metamodels were established mainly by using static design of experiment (DOE) methods [30,31] together with individual metamodeling methods [20] in these studies. Sun et al. [21] and Yin et al. [22] all established the metamodels of SEA and PCF for functionally graded foam (FGF) structures by means of separating the design space. However, it is very troublesome to establish the metamodels by separating the design space [21,22]. The optimal objectives such as specific energy absorption (SEA) and peak crushing force (PCF) of FGF-filled thin-walled structures always perform highly nonlinear characteristics because of the effect of density gradient [21–23]. Thus, it is still hard to establish accurate metamodels for these optimal objectives of FGF-filled thin-walled structures without separating the design space by using a certain number of design points [21,22].

In this paper, the new structure of functionally graded foam-filled tapered tubes (FGFTT) is firstly proposed and investigated by nonlinear finite element analysis (FEA) through LS-DYNA. Furthermore, in order to seek for the optimal designs of FGFTT, a new kind of multiobjective crashworthiness optimization method by jointly using the dynamic DOE method [32–35], the ensemble metamodeling method [36–38] and the multiobjective particle swarm optimization (MOPSO) algorithm is presented. In the optimization process of this new method, the accurate metamodels called as dynamic ensemble metamodel for the optimal objectives of FGFTTs are first established without separating the design space. Then, FGFTTs are optimized by employing the MOPSO algorithm to achieve maximum SEA and minimum PCF with the dynamic ensemble metamodels. After that, the Pareto fronts for the conflicting objectives SEA and PCF are obtained. From the Pareto fronts, we can obtain a series of optimal designs of FGFTTs which can satisfy different practical design conditions for crashworthiness.

2. Structural crashworthiness indicators

In order to study the crashworthiness of energy absorbed structures, it is essential to define the crashworthiness indicators. There are many different indicators available to evaluate the energy absorption capabilities of different structures [39]. Among these indicators, specific energy absorption (SEA) is usually used to estimate the energy absorption capacity of absorbers. SEA is defined as the ratio of the absorbed energy to the mass of the structure and it can be formulated as [40]:

$$\mathrm{SEA}(d) = \frac{\mathrm{EA}(d)}{M}, \tag{1}$$

where d is the axial crushing distance. M is the total mass of the structure and EA is total absorbed energy during crushing, which can be calculated as:

$$\mathrm{EA}(d) = \int_0^d F(x)\mathrm{d}x, \tag{2}$$

where F denotes the axial crushing force. Obviously, the higher the SEA, the better the energy absorption capacity of a structure.

In the design of energy absorption structures which is used to absorb the impact energy in collision, another important indicator is the peak crushing force (PCF) of the energy absorption structure. Taking the vehicle crashworthiness as example, the PCF of the absorber may determine the occupant survival rate when impact occurs. A large PCF often leads to a high deceleration and may cause severe injury or even death of occupant [41]. The axial crushing force–displacement curve of a typical foam-filled tapered structure is shown in Fig. 1 [20]. As shown in Fig. 1, the PCF occurs in the end of the curve, which is different from that of the hollow thin-walled structure. The Peak crushing forces of typical hollow thin-walled structure and foam-filled tapered thin-walled structure are respectively marked as the red solid circle 1 and 2 in Fig. 1, when the crushing distances at the left side of the dashed line are considered.

3. Finite element modeling of FGFTT

3.1. Finite element model

The geometrical configuration of the FGFTT considered in our study is shown in Fig. 2, which is actually a tapered cylinder tube filled with functionally graded aluminum foam. In our study, some structure parameters of a FGTT are fixed to illustrate the analysis process. The radius R_1 of the top circle and the radius R_2 of the bottom circle of the tapered cylinder tube are fixed as 40 mm and 60 mm, respectively. The thickness t and the length L of the tube are 2 mm and 240 mm, respectively. The geometry of the tube is determined from the dimensions of a typical lower rail of a passenger car [40]. In order to simulate the front crash of a passenger car, the functionally graded foam-filled tapered tube (FGFTT) impacts onto a rigid wall at an initial velocity of 15 m/s with an additional mass of 600 kg attached to its bottom end in our study as shown in Fig. 2.

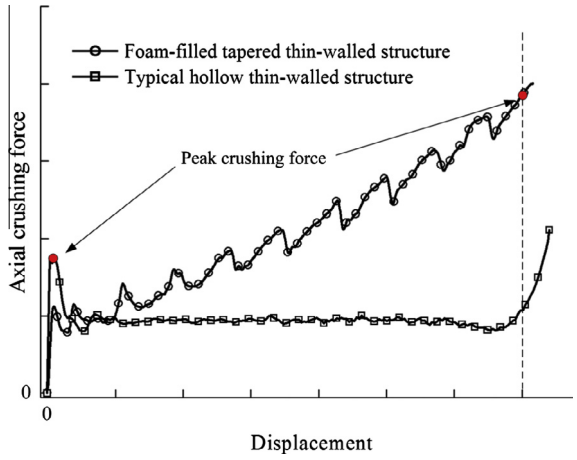

Fig. 1. Axial crushing force–displacement curves of energy absorbed structures.

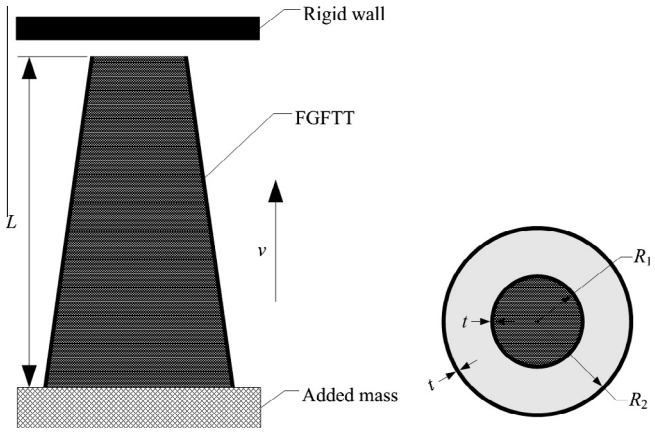

Fig. 2. Geometrical configuration of FGFTT and its loading conditions.

The tapered tube is modeled using Belytschko-Tsay four-node shell elements with three integration points through the thickness and one integration point in the element plane. The functionally graded foam (FGF) is meshed with eight-node solid elements with one-point reduced integration. An automatic node-to-surface contact is chosen to simulate the contact between the specimen and the rigid wall. An automatic single-surface contact is adopted to simulate the buckling of the FGF and the tube under axial dynamic loading. In these contacts, the static and dynamic coefficients of frictions are 0.20 [42]. In our study, the adhesive between the FGF and the tube is considered [43]. The interface between the FGF and the tube is simulated using a tiebreak-contact model. In this tiebreak-contact model, sliding is not allowed from node to node until the tensile or shear stress exceeds the ultimate strength. But if the tensile or shear stress exceeds the tensile and shear ultimate strength, the bonding will fail and the contact will automatically behave as a surface-to-surface contact. The failure is determined by the following criterion [44,45]:

$$\left[\frac{\sigma}{\sigma_f}\right]^2 + \left[\frac{\tau}{\tau_f}\right]^2 \le 1, \tag{3}$$

where σ_f and τ_f are tensile and shear ultimate strength of the adhesive material, respectively. In this study, we have $\sigma_f = 150$ MPa and $\tau_f = 150$ MPa [43].

From the above described finite element modeling method, the three dimensional finite element model of FGFTT is established by employing the explicit nonlinear finite element software LS-DYNA as shown in Fig. 3.

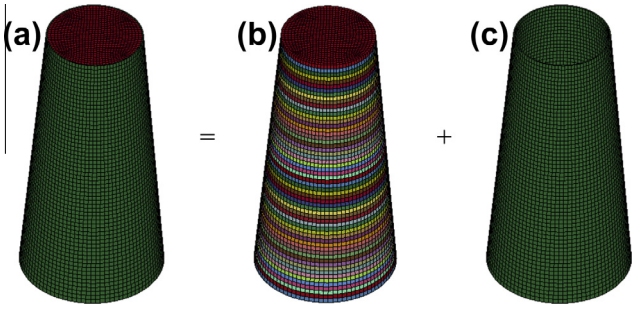

Fig. 3. Finite element model of FGFTT: (a) FGFTT, (b) FGF filler and (c) tapered cylinder tube.

3.2. Material properties

The material of the tapered cylinder tube here is aluminum alloy AA6060 T4 with mechanical properties of density $\rho = 2.7 \times 10^3$ kg/m^3, Young's modulus $E = 68.2$ GPa, initial yield stress $\sigma_y = 80$ MPa, ultimate stress $\sigma_u = 173$ MPa, Poisson's ratio $\mu = 0.3$ and power law exponent $n = 0.23$ [5]. The tensile stress–strain curve is shown in Fig. 4. The constitutive behavior of the tube is based on an elastic–plastic material model with von Mises's isotropic plasticity algorithm. In this material constitutive model, plastic hardening is defined by several piecewise lines. The effect of strain rate in this model is neglected due to the insensitivity of strain rate of aluminum alloy material [46].

Functionally graded foam (FGF) is a new kind of filler material. In order to enhance the crashworthiness of the aluminum alloy tapered tube, it is filled with FGF. The density gradient of the filled foam is along the axial direction of the tube. In our study, the density gradient is determined by the following power-law function as [21,22]:

$$\rho_{\mathrm{FGF}}(x) = \rho_{\max} + (\rho_{\min} - \rho_{\max})\left(\frac{x}{L}\right)^m, \tag{4}$$

where $\rho_{\max}$ and $\rho_{\min}$ are the maximum and minimum densities of the FGF, respectively. As shown in Fig. 5, x is the distance from the top surface of the FGF and L is the length of the tapered tube. m is the graded parameter that governs the variation of foam density. As shown in Fig. 5, two kinds of FGFs described as descending grading pattern and ascending grading pattern are investigated in this study. However, there is no effective constitutive model available for functionally graded foam materials. In order to deal with this problem, the foam is divided into 60 layers along the direction of grading [21]. The height of each layer is equal to the length of the meshed solid element. Each layer is considered as an isotropic uniform foam material whose constitutive behavior is based on as an isotropic uniform material model developed by Deshpande and Fleck [47]. The yield criterion of this material is defined as:

$$\Phi = \sigma_e - Y \le 0, \tag{5}$$

where Φ denotes the yield surface. Y is the yield strength and σ_e is an equivalent stress, which is given as:

$$\sigma_e^2 = \frac{1}{1 + (\alpha/3)^2}(\sigma_v^2 + \alpha^2\sigma_m^2), \tag{6}$$

where σ_v and σ_m represent the von Mises effective stress and the mean stress, respectively. α is a parameter which can determine the shape of the yield surface and it can be written as

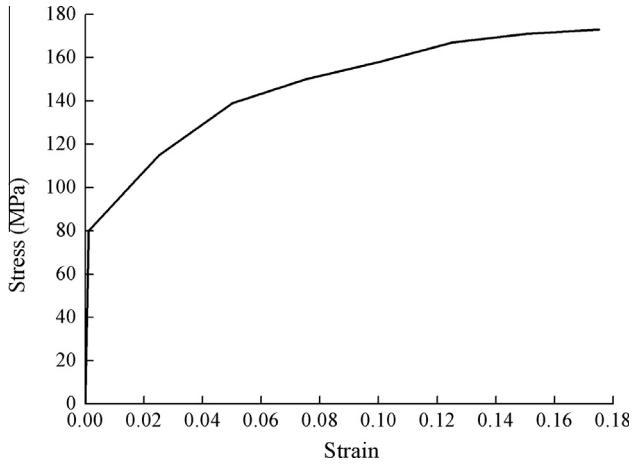

Fig. 4. Tensile stress–strain curve of AA 6060 T4 [5].

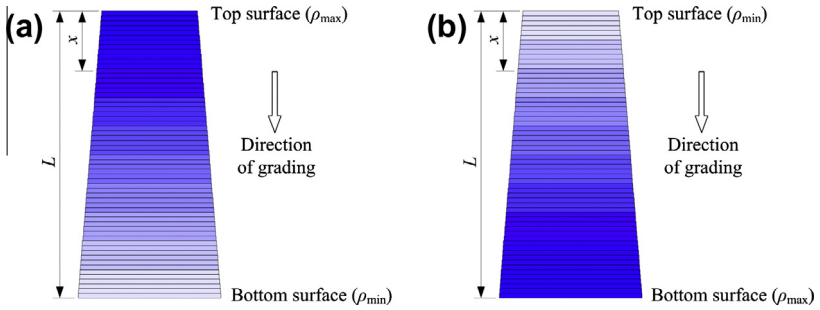

Fig. 5. Schematic of density grading patterns for the FGF: (a) descending grading pattern, and (b) ascending grading pattern.

$$\alpha^2 = \frac{9(1-2\nu^p)}{2(1+\nu^p)}, \tag{7}$$

where ν^p is the plastic coefficient of contraction. For the aluminum foam, $\nu^p = 0$ in most cases, then $\alpha = 2.12$.The strain hardening rule is adopted in this material model as:

$$Y = \sigma_p + \gamma \frac{\varepsilon_e}{\varepsilon_D} + \alpha_2 \ln\left[\frac{1}{1-(\varepsilon_e/\varepsilon_D)^\beta}\right], \tag{8}$$

where ε_e is the equivalent strain. σ_p, α_2, γ, β and ε_D are material parameters and can be expressed as functions of the foam density.

$$\begin{cases} \left(\sigma_p, \alpha_2, \gamma, \frac{1}{\beta}, E_p\right) = C_0 + C_1\left(\frac{\rho_f}{\rho_{f0}}\right)^q, \\ \varepsilon_D = -\frac{9+\alpha^2}{3\alpha^2}\ln\left(\frac{\rho_f}{\rho_{f0}}\right) \end{cases} \tag{9}$$

where ρ_f and ρ_{f0} denote the foam density and the base material density, respectively. C_0, C_1 and q are constants, which are given in Table 1. It can be found from Eq. (9) that E_p is also a function of the foam density.

Fracture is considered in this model by removing (eroding) elements when they reach a critical strain. The volumetric strain ε_m, which is positive in tension and negative in compression, is chosen as a measure for when an element should be eroded. If $\varepsilon_m \geq \varepsilon_m^{cr}$, the element will be eroded. ε_m^{cr} means the critical volumetric strain and is defined as 0.1 in our study [46].

4. Numerical simulation results and discussion

4.1. Validation of the finite element model

The finite element model of the FGFTT is very difficult to be directly validated as the experimental data have yet to be reported adequately. However, it is possible to validate the simulation results of uniform foam-filled cylinder tube, which is a special case of FGFTT with $m = 0$ and $R_1 = R_2$. Hanssen et al. had carried out a lot of axial dynamic loading experiments for investigating the crash behaviors of cylinder AA6060 T4 aluminum tubes filled with aluminum foam [6]. In this study, the experimental results obtained by Hanssen et al. are employed to validate the numerical results of FGFTTs in the special case. The comparison of the axial crushing force versus displacement of the FGFTT ($m = 0$ and $R_1 = R_2$) between the finite element analysis (FEA) and experimental results with $\rho_f = 0.13$ g/cm^3 and $v = 15.1$ m/s are shown in Fig. 6. It can be found from Fig. 6 that the axial crushing force of the FEA result is in good agreement with the experimental result. This satisfactory correlation provides adequate evidence for extending the uniform foam-filler model ($m = 0$ and $R_1 = R_2$) to the FGF filler models (m equals any other values and $R_1 \neq R_2$), which will be used in our following study.

Table 1
Material constants for aluminum foam [48,49].

	σ_p (MPa)	α_2 (MPa)	$1/\beta$	γ (MPa)	E_p (MPa)
C_0 (MPa)	0	0	0.22	0	0
C_1 (MPa)	720	140	320	42	0.33×10^6
q	2.33	0.45	4.66	1.42	2.45

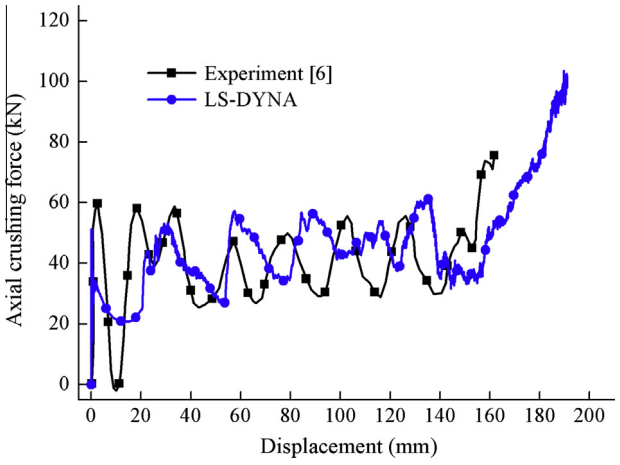

Fig. 6. Crushing force versus displacement of the FGF filled tube ($m = 0$ and $R_1 = R_2$).

4.2. Crashworthiness comparison of uniform foam and FGF filled tapered tube

In order to compare the energy absorption capacity of uniform foam-filled tapered tubes (UFTT) with that of FGFTTs with the same weight, numerical simulations are implemented based on the finite element models of FGFTTs with different values of parameter m. In this study, the value of parameter m increases from 0 to 10 and each value of parameter m corresponds to one case. The deformation for calculating the energy absorption of the FGFTT is chosen as 140 mm, which is about 60 percent of the total length of the specimen. To be consistent, $\rho_{max} = 0.5$ g/cm^3 and $\rho_{min} = 0.3$ g/cm^3 for all the FGFTTs. In order to keep the same weight as the FGFTT, the density of filled foam of UFTT is calculated as:

$$\rho_{UF} = \frac{1}{V_{UF}}\sum_{i=1}^{N}\rho_{FGF\_i}V_{FGF\_i}, \tag{10}$$

where ρ_{FGF_i} and V_{FGF_i} are the density and volume of the ith layer of the FGFs, respectively. P_{UF} and V_{UF} denote the density and volume of the UF, respectively. N is the number of the layers of the FGFs. In this paper, N equals to 60. According to Eq. (4), the density of FGF ρ_{FGF_i} is determined by parameter m. Thus, the density of UF ρ_{UF}

will vary with the value of parameter m. It is easy to find that the foam densities of UFTTs increase with decreasing m. The lowest density of the foam is 0.3 g/cm^3 when m equals to 0.

Fig. 7 shows the relationship between SEA and m of the functionally graded foam-filled tapered tube with ascending grading pattern (FGFTT-AGP) and the corresponding UFTT. It can be clearly found that SEA of FGFTT-AGP is smaller than that of the corresponding UFTT. Instead, PCF of the FGFTT-AGP is bigger than that of the corresponding UFTT, which can be clearly seen from Fig. 8. According to the comparison results of SEA and PCF, we can easily find that the crashworthiness of the FGFTT-AGP is worse than that of the corresponding UFTT.

Fig. 9 plots the relationship between SEA and m of the functionally graded foam-filled tapered tube with descending grading pattern (FGFTT-DGP) and the corresponding UFTT. From Fig. 9, we can find that SEA of FGFTT-DGP is obviously bigger than that of the corresponding UFTT. In addition, the comparison of PCF between the FGFTT-DGP and the corresponding UFTT is given in Fig. 10. It can be seen from Fig. 10 that PCF of the FGFTT-DGP is smaller than that of the corresponding UFTT when m is less than 1. An opposite result can be observed when m is larger than 1 except for the cases of m = 6 and 7.5. Based on the above comparison, the crashworthiness of FGFTT-DGP is generally better than that of the corresponding UFTT. Thus, the FGFTTs-DGP can be used as excellent energy absorbers in vehicle engineering in future. However, it can be found from the above study that the graded parameter m significantly influence the crashworthiness of FGFTTs-DGP. Therefore, it is of great importance to seek the best value of parameter m for optimizing the crashworthiness of the FGFTTs-DGP. This will be carried out in the following study.

5. Multiobjective design optimization

5.1. Optimization problem set-up

As an energy absorber, the structure is expected to absorb as much impact energy as possible per unit mass. Thus, SEA should be chosen as an objective function and maximized in the crashworthiness optimization problem. On the other hand, PCF of the structure is another very importance indicator for the safety of the crushed object. PCF of the structure should be constrained under a certain level. Thus, PCF is set as another objective function and minimize it in the optimization problem. To account for these two different design criteria, the optimization problem can be written as the following multiobjective optimization form:

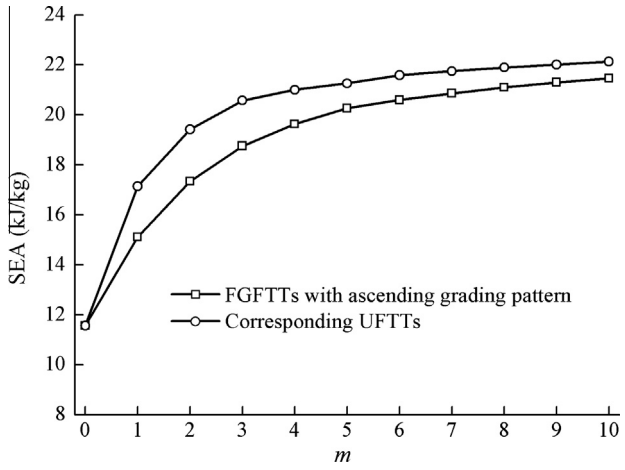

Fig. 7. SEA versus m of the FGFTTs-AGP and the corresponding UFTTs.

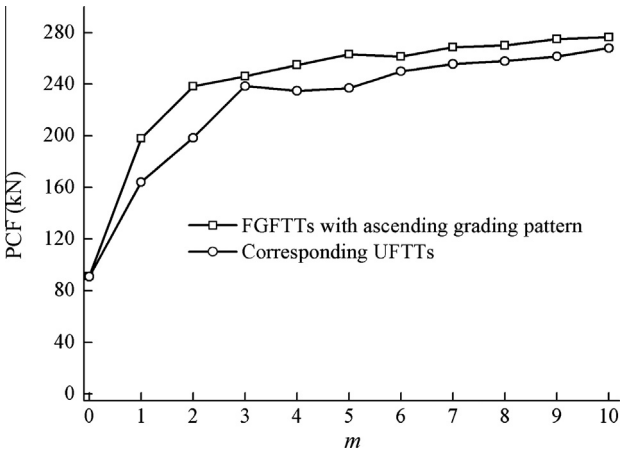

Fig. 8. PCF versus m of the FGFTTs-AGP and the corresponding UFTTs.

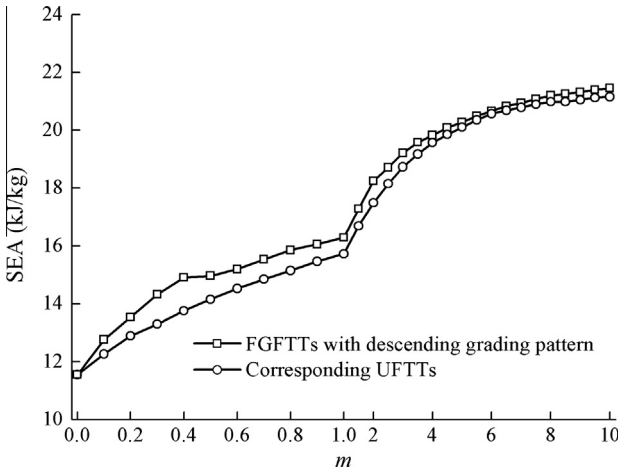

Fig. 9. SEA versus m of the FGFTTs-DGP and the corresponding UFTTs.

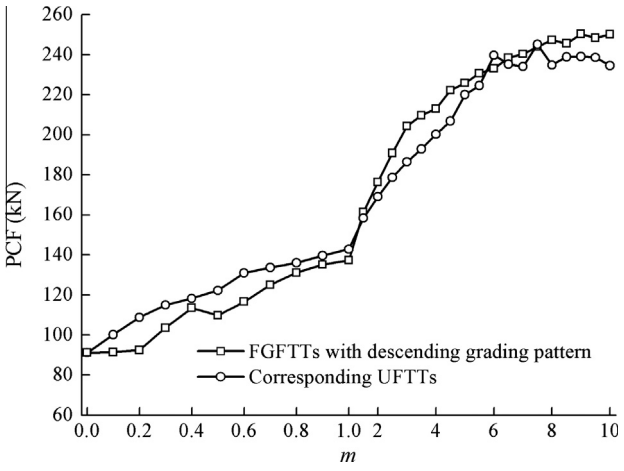

Fig. 10. PCF versus m of the FGFTTs-DGP and the corresponding UFTTs.

$$\begin{cases} \text{Minimize } \{\text{PCF}(m), -\text{SEA}(m)\}, \\ \text{Subject to } m_{\text{L}} \le m \le m_{\text{U}}, \end{cases} \tag{11}$$

where m is the gradient parameter, m_{L} and m_{U} are the lower limit and upper limit of parameter m, respectively. In this paper, m_{L} and m_{U} are selected as 0 and 10, respectively. According to Figs. 9

and 10, both PCF(m) and SEA(m) exhibit nonlinear characteristics. In order to fit the two objective functions well, a dynamic ensemble metamodeling method is presented and used in the following multiobjective design optimization (MDO). The flowchart of the implementation of the MDO in this study is shown in Fig. 11 [50–52]. In the process of this new multiobjective crashworthiness optimization method, a most important step is the dynamic ensemble metamodeling. The iteration of this important step will terminate only if the accuracy of metamodel is satisfied or the number of total samples exceeds user-defined maximum value or the number of iteration exceeds user-defined maximum iteration number.

5.2. Dynamic ensemble metamodeling method

In this work, the design of experiment (DOE) for sampling initial points is implemented using the optimal Latin hypercube design (OLHD) method [53]. The OLHD method adds a distribution criterion to the LHD [53]. Thus, the distribution of OLHD sample points is really evener than that of LHD in the design space.

In order to reduce the computational cost, metamodels are extensively used in the optimization design. Previous research has demonstrated several metamodels such as polynomial response surface (PRS), radial basis function (RBF), Kriging (KRG), support vector regression (SVR), multivariate dynamic regression splines (MARS) et al. [54]. Different metamodels are suitable for fitting different functions. Each metamodel has its advantage and also has its drawback [54]. Thus, an ensemble of metamodels would be a good choice for fitting black-box functions for most engineering problems. An ensemble is firstly constructed using a weighted average surrogate (WAS) models by Goel et al. [36]. It consists of PRS, RBF and KRG, and provides different prediction capability. The prediction of an ensemble surrogate can be formulated as:

$$\hat{y}_{\text{ens}}(\mathbf{x}) = \sum_{i=1}^{M} w_i \hat{y}_i(\mathbf{x}), \tag{12}$$

where $\mathbf{x}$ is the vector of design variables, $\hat{y}_{\text{ens}}$ is the ensemble prediction, $\hat{y}_i$ is the prediction by the ith metamodel, M is the number of basic metamodels used for ensemble metamodel construction and w_i is the weight of the ith metamodel. The sum of weights must be equals to 1. A metamodel that is deemed more accurate should be assigned a large weight, and the less accurate model should have less influence on the predictions. There are many possible strategies

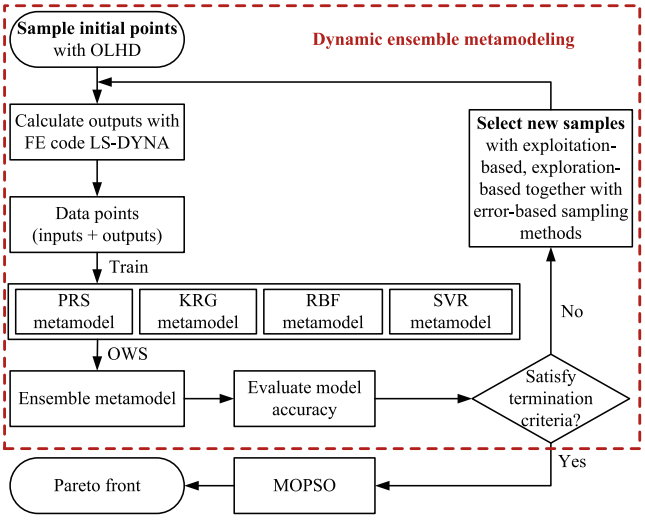

Fig. 11. Flowchart of MDO with dynamic ensemble metamodel.

of selecting weights [36]. An optimal weighted surrogate (OWS) scheme [37] is recognized as an effective method for determining the weights of the ensemble surrogate. The weights w_i can be obtained by solving an optimization problem as:

$$\begin{cases} \text{Minimize } \text{GMSE}_{\text{ens}} = \frac{1}{N_{\text{tra}}} \sum_{i=1}^{N_{\text{tra}}} (y_i - \hat{y}_i^{\text{ens}})^2, \\ \text{Subject to } \sum_{i=1}^{M} w_i = 1, \end{cases} \tag{13}$$

where N_{tra} is the number of training points. y_i and $\hat{y}_i^{\text{ens}}$ denote the real value and the prediction value by the ensemble metamodel of ith training point, respectively. GMSE_{ens} denotes the generalized mean square error (GMSE) of the ensemble metamodel. GMSE is calculated using leave-one-out cross-validation strategy. If there are N_{tra} training points, then a metamodel is constructed N_{tra} times, each time leaving out one of the training points. In our work, four individual metamodels PRS, RBF, KRG and SVR are used to construct the ensemble metamodel.

PRS [55,56] is considered appropriate in the design optimization problems involving complex nonlinear mechanics like contact-impact. In this approach, an approximation $\hat{y}(\mathbf{x})$ to the structural responses is assumed a priori in terms of the polynomial function in a form of:

$$\hat{y}_{\text{PRS}}(\mathbf{x}) = \sum_{i=1}^{k} a_i \varphi_i(\mathbf{x}), \tag{14}$$

where k is the number of polynomial function $\varphi_i(\mathbf{x})$ and $\mathbf{x}$ is the vector of design variables. For instance, the quadratic polynomial response surface with two variables can be expressed as follows:

$$\hat{y}_{\text{PRS}} = a_1 + a_2 x_1 + a_3 x_2 + a_4 x_1^2 + a_5 x_2^2 + a_6 x_1 x_2. \tag{15}$$

By respectively replace $x_1^2, x_2^2, x_1 x_2$ with x_3, x_4, x_5, Eq. (15) will become a linear regression model as follows:

$$\hat{y}_{\text{PRS}} = a_1 + a_2 x_1 + a_3 x_2 + a_4 x_3 + a_5 x_4 + a_6 x_5. \tag{16}$$

According to Eq. (16), a matrix expression can be written as:

$$\mathbf{Y} = \mathbf{\Phi A} + \mathbf{E}. \tag{17}$$

where

$$\mathbf{Y} = \begin{bmatrix} y_1 \\ y_2 \\ \vdots \\ y_n \end{bmatrix}, \mathbf{\Phi} = \begin{bmatrix} 1 & x_{11} & x_{12} & \cdots & x_{1k} \\ 1 & x_{21} & x_{22} & \cdots & x_{2k} \\ \vdots & \vdots & \vdots & \ddots & \vdots \\ 1 & x_{n1} & x_{n2} & \cdots & x_{nk} \end{bmatrix}, \mathbf{A} = \begin{bmatrix} a_1 \\ a_2 \\ \vdots \\ a_n \end{bmatrix}, \mathbf{E} = \begin{bmatrix} e_1 \\ e_2 \\ \vdots \\ e_n \end{bmatrix}. \tag{18}$$

where n is the number of training points. $\mathbf{Y}$ is the vector of the values of the training points. $\mathbf{E}$ is an error vector and the unbiased estimator of the coefficient vector $\mathbf{A}$. By using the well-known least square error method, the coefficient vector $\mathbf{A}$ can be obtained as:

$$\mathbf{A} = (\mathbf{\Phi}^{\text{T}} \mathbf{\Phi})^{-1} \mathbf{\Phi}^{\text{T}} \mathbf{Y}. \tag{19}$$

RBF is originally developed by Hardy [57] to fit irregular topographic contours of geographical data. Now, RBF has been used in many problems. For the approximation of the objective function $y(\mathbf{x})$, RBF has the following mathematical form as:

$$\hat{y}_{\text{RBF}}(\mathbf{x}) = \sum_{i=1}^{N_{\text{tra}}} r_i \phi(\|\mathbf{x} - \mathbf{x}_i\|), \tag{20}$$

where $\mathbf{x}_i$ is the vector of design variables at the ith training points, $\|\mathbf{x} - \mathbf{x}_i\|$ is the Euclidean distance, r_i is the coefficient of the linear combination of N_{tra} neurons and ϕ is a basis function.A KRG model

can be expressed as a combination of a global model and an additive localized approximation as [58,59]:

$$\hat{y}_{KRG}(\mathbf{x}) = g(\mathbf{x}) + z(\mathbf{x}), \tag{21}$$

where $g(\mathbf{x})$ is a known polynomial function of $\mathbf{x}$ as a global model of the original function, and $z(\mathbf{x})$, which represents a local deviation from the global model, is a correlation function with zero mean value and non-zero covariance.

SVR [60] is a recently developed regression method. It is capable of solving nonlinear problems using kernel functions and has been successful in various domains [61]. Considering a set of data $\{(\mathbf{x}_i, y_i), i = 1, 2,.. ., N_{tra}\}$, where $\mathbf{x}_i$ is the vector of inputs, y_i is the corresponding output, the aim of SVR like any other regression methods is to determine a function $y(\mathbf{x})$, which can accurately predict the desired output y at any input $\mathbf{x}$. In SVR, the input $\mathbf{x}$ is first mapped into a higher-dimensional feature space $\boldsymbol{F}$ via a nonlinear mapping function $k(\mathbf{x})$ and then the regression is carried out in this space. Generally, the SVR gives the regression function in the following form as [62].

$$\hat{y}_{SVR}(\mathbf{x}) = \mathbf{w} \cdot k(\mathbf{x}) + b, \tag{22}$$

where $\mathbf{w}$ is a weight vector, b is a constant, and $(\cdot)$ denotes the dot production in the feature space $\boldsymbol{F}$.

Another important step in constructing the dynamic ensemble metamodel is selecting new samples. The sampling new points technique in our study is a hybrid of the exploitation-based (filling up the design space as equally as possible) sampling method, the exploration-based (selecting data points in highly nonlinear regions) sampling method and the error-based (selecting points in locations where the model error is estimated to be the largest) sampling method. It uses an exploitation criterion based on LOcal Linear Approximations (LOLA) of the system and an exploration criterion using a Voronoi tessellation of the design space. LOLA-Voronoi is a highly dynamic sampling algorithm which performs a trade-off between exploration and exploitation. For more detailed information on the (mathematical) principles of LOLA-Voronoi tessellation and its implementation, please refer to Refs. [50–52].

5.3. Accuracy evaluation and multiobjective optimization algorithm

The accuracy of the metamodels can be evaluated based on the root mean square error (RMSE) and the relative error (RE), respectively, which are written as:

$$\mathrm{RMSE} = \sqrt{\frac{1}{N_{val}}\sum_{i=1}^{N_{val}}(y_i - \hat{y}_i)^2}, \tag{23}$$

$$\mathrm{RE} = \frac{y_i - \hat{y}_i}{y_i}. \tag{24}$$

where N_{val} is the number of validation points. y_i and $\hat{y}_i$ are the FEA result and the approximate result by metamodel, respectively. RMSE is used to gauge the overall accuracy of the model, while RE is used to gauge to local accuracy of the model. In our study, we used validation points to evaluate the metamodels.

Based on the dynamic ensemble metamodels which are accurate enough, the implementation of multiobjective optimization of the crashworthiness of FGFTT becomes feasible. In comparison with other multiobjective optimization algorithms such as NSGA [63] and PEAS approaches [64,65], the multiobjective particle swarm optimization (MOPSO) that incorporates the mechanism of crowding distance computation has drawn considerable attention recently due to its relatively fast convergence and well-distributed Pareto front. The details of MOPSO can be consulted from Ref. [64]. In this paper, the MOPSO algorithm is employed to obtain the Pareto front of the two conflicting objectives of SEA and PCF. The Pareto front is actually a set of the non-dominated optimal solutions. The engineers can make their own decision according to the actual demand from the obtained Pareto front [63].

5.4. MDO of FGFTTs-DGP

In order to establish the metamodels of SEA and PCF of FGFTT-DGP, 21 design points are sampled using the full-factorial static DOE method [30]. These design points and the corresponding response values are listed in Table 2. According to the methodology described in Section 5.2, five different metamodels (PRS, RBF, KRG, SVR and Ensemble) with full-factorial static DOE method for FGFTTs-DGP are established using 21 design points. The order of polynomial functions of PRS in our study is chosen as 3 [20]. In order to evaluate the accuracies of these metamodels, 10 additional points shown in Table 3 are used. Based on Section 5.3, the accuracy evaluation indicators of these metamodels are calculated and summarized in Table 4. From Table 4, we can find that the ensemble metamodels of SEA and PCF are the most accurate ones among those metamodels of SEA and PCF, respectively.

In addition, we established the dynamic ensemble metamodels of SEA and PCF of FGFTTs-DGP using the dynamic ensemble metamodeling method described in Sections 5.1 and 5.2. In order to compare the accuracies of the dynamic ensemble metamodels with the static ensemble metamodels, an equal number of design points are sampled in the dynamic ensemble metamodeling process. These design points obtained by dynamic DOE method are listed in Table 2. The comparison of the accuracies of ensemble metamodels with different DOE methods is shown in Table 5. From Table 5, it can be found that the dynamic ensemble metamodel is more accurate than the static ensemble metamodel in terms of RMSE. This indicates that the dynamic ensemble metamodel is the most accurate one among all the established metamodels in this study. The relative errors of the dynamic ensemble metamodels of SEA and PCF are less than 2%, which is acceptable in engineering design. The plots of the dynamic ensemble metamodels of PCF and SEA for FGFTTs-DGP are given in Fig. 12(a) and (b), respectively. From Fig. 12, it can be seen that the dynamic ensemble metamodels of SEA and PCF both predict the objective function values very well.

Based on the dynamic ensemble metamodels of SEA and PCF, the Pareto fronts of FGFTTs-DGP for the optimization problem defined as Eq. (11) is obtained and shown in Fig. 13 by using the MOPSO algorithm. The optimal design (PCF constrained under 120 kN) of the FGFTTs-DGP corresponds to the Pareto point marked as solid circle in Fig. 13. The detailed design parameter of the optimal design is listed in Table 6. In addition, the detailed design parameters of the optimal designs (PCF constrained under 120 kN) of the FGFTTs-DGP based on the Pareto fronts, which are obtained by using the static metamodels and the MOPSO algorithm, are also listed in Table 6. Then, the finite element models for the optimal designs are established. The comparison between the FEA results and the approximate results are shown in Table 6. From Table 6, we can find that the errors of SEA and PCF of the optimal design obtained by using dynamic ensemble metamodels are less than 1% and the optimal design satisfies the constraint condition. However, the PCFs of the optimal designs by using static RBF, static SVR and static ensemble metamodels both exceed the constraint value of 120 kN. And, the overall errors between FEA and traditional static metamodels of the optimal designs are bigger than that of the optimal designs obtained by dynamic ensemble metamodels. This indicates that the dynamic ensemble

Table 2
Design points by static and dynamic DOE.

Static DOE				Dynamic DOE			
No.	m	SEA (kJ/kg)	PCF (kN)	No.	m	SEA (kJ/kg)	PCF (kN)
1	0.0000	11.5567	91.2204	1[a]	0.0000	11.5561	91.0330
2	0.5000	14.9643	109.7708	2[b]	0.1017	12.8086	91.7439
3	1.0000	16.2929	137.2717	3[b]	0.2061	13.5939	94.1283
4	1.5000	17.2864	161.3103	4[b]	0.3937	14.8960	113.8890
5	2.0000	18.2459	176.3429	5[b]	0.4094	14.8466	110.4376
6	2.5000	18.7122	190.8175	6[b]	0.5314	15.0279	115.5240
7	3.0000	19.2102	204.2699	7[b]	0.7010	15.5387	124.9771
8	3.5000	19.5774	209.6757	8[a]	1.0000	16.2931	137.2638
9	4.0000	19.8302	212.9776	9[b]	1.5844	17.4614	164.6300
10	4.5000	20.0922	222.1964	10[a]	2.0000	18.2452	176.2596
11	5.0000	20.2772	225.8012	11[b]	2.4609	18.6573	190.6271
12	5.5000	20.4929	230.6620	12[a]	3.0000	19.2100	204.3404
13	6.0000	20.6610	233.0707	13[b]	3.4902	19.5776	207.8110
14	6.5000	20.8369	238.5589	14[a]	4.0000	19.8308	215.7685
15	7.0000	20.9409	240.4038	15[a]	5.0000	20.2771	224.8584
16	7.5000	21.0782	243.9127	16[a]	6.0000	20.6584	234.8966
17	8.0000	21.1972	247.3878	17[a]	7.0000	20.9432	239.3533
18	8.5000	21.2570	245.6600	18[a]	8.0000	21.1966	247.6603
19	9.0000	21.3166	250.3562	19[a]	9.0000	21.3244	249.6001
20	9.5000	21.3928	248.4098	20[b]	9.8276	21.4278	249.5431
21	10.000	21.4517	250.1992	21[b]	10.000	21.4515	249.9099

[a] Denote the initial design points in dynamic DOE, respectively.
[b] Denote the updated design points in dynamic DOE, respectively.

Table 3
Validation points.

No.	*m*	SEA (kJ/kg)	PCF (kN)	No.	*m*	SEA (kJ/kg)	PCF (kN)
1	0.8000	15.8527	131.0265	6	5.8000	20.6120	234.2121
2	1.8000	17.8187	172.5557	7	6.8000	20.8932	238.7484
3	2.8000	18.9759	197.9653	8	7.8000	21.1507	245.4770
4	3.8000	19.7351	213.6379	9	8.8000	21.2813	246.6768
5	4.8000	20.1904	220.5344	10	9.8000	21.4355	250.2245

Table 4
Accuracies of different metamodels with static DOE.

	SEA		PCF	
Metamodels	RMSE	RE (%)	RMSE	RE (%)
PRS	0.3056	[−1.6658, 4.1569]	3.0622	[−3.0256, 2.9525]
RBF	0.0603	[−0.4835, 0.7304]	2.6904	[−1.8529, 3.9739]
KRG	0.0431	[−0.6112, 0.0785]	2.7345	[−1.8823, 3.8721]
SVR	0.0392	[−0.5147, 0.0790]	2.6330	[−1.8714, 3.9777]
Ensemble	0.0281	[−0.3592, 0.0832]	2.3328	[−2.3116, 2.9335]

Table 5
Accuracies of ensemble metamodels with different DOE methods.

	SEA		PCF	
DOE methods	RMSE	RE (%)	RMSE	RE (%)
Static	0.0281	[−0.3592, 0.0832]	2.3328	[−2.3116, 2.9335]
Dynamic	0.0266	[−0.3281, 0.1799]	1.5886	[−1.3131, 1.5086]

metamodeling method is more suitable for the multiobjective crashworthiness design in engineering than the traditional static metamodeling methods. However, from the FEA results of Table 6, it seems that the static KRG generates the best design of FGFTT-DGP with satisfied constraint though its global accuracy is not as high as the dynamic ensemble metamodel. The reason for this is most possibly that the local accuracy of static KRG in the small design space around the optimal design is higher than that of the dynamic ensemble metamodel. Thus, the metamodel with the highest accuracy may not necessarily generate the best design. To find the real optimum design, it is necessary to implement simultaneous tests of multiple metamodels [20].

In order to compare the crashworthiness of FGFTT-DGP with that of the UFTT, the Pareto front of UFTT which is obtained by MOPSO algorithm and the metamodels is also given in Fig. 13. To simplify the metamodeling process, the static 7th-order PRS metamodels of SEA and PCF for UFTT are used [22]. The detailed metamodeling method for static PRS models is shown in Section 5.2. From Fig. 13, it can be found that the crashworthiness of FGFTT-DGP is obviously better than that of the UFTT with the same weight when the constraint of PCF < 180 kN. On the contrary, the crashworthiness of FGFTT-DGP is a little worse than that of the UFTT with the same weight when the constraint of PCF > 180 kN. However, the Pareto points of the FGFTTs-DGP and the UFTTs are very close when the constraint of PCF > 180 kN. As a whole, the SEA of FGFTT-DGP is bigger than that of the UFTT in most values of the constraint PCF. In other word, the crashworthiness of FGFTT-DGP is better than that of the UFTT with the same weight in most of the considered cases.

From Table 6, the corresponding parameter *m* of the optimal design of FGFTT-DGP obtained by dynamic ensemble metamodel is 0.560 when PCF is constrained under 120 kN. The force–displacement curve of this optimal design obtained by FEA is plotted in Fig. 14. It can be found that the PCF of FGFTT-DGP compressed by 140 mm is close to but less than 120 kN. The force–displacement curve of the corresponding UFTT with the same weight as the optimal design of FGFTT-DGP is also plotted in Fig. 14. The SEA and PCF of the corresponding UFTT are 14.4013 kJ/kg and 129.2253 kN, respectively. By comparing the crashworthiness indicators of the optimal design of the FGFTT-DGP with that of the corresponding UFTT, we find that the crashworthiness of the optimal design of FGFTT-DGP is better than that of the corresponding UFTT. This further indicates that the FGFTT-DGP is a new kind of

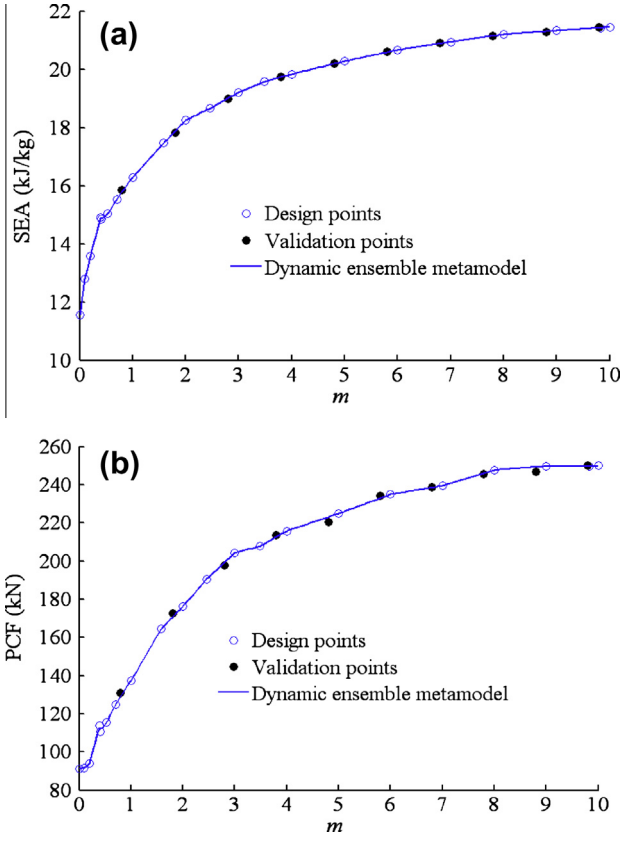

Fig. 12. Dynamic ensemble metamodels of SEA and PCF for FGFTTs-DGP: (a) SEA and (b) PCF.

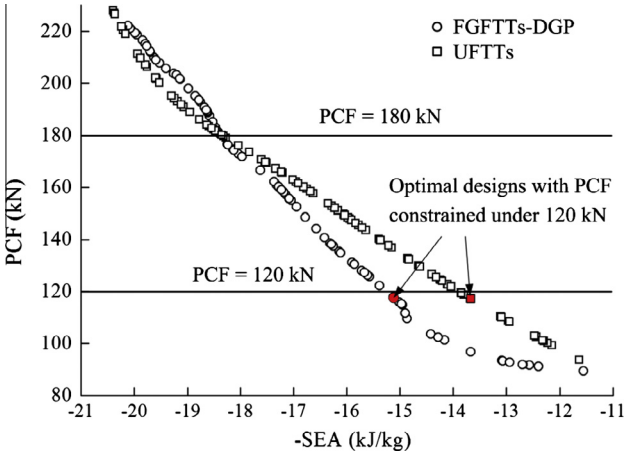

Fig. 13. Pareto front of FGFTTs-DGP.

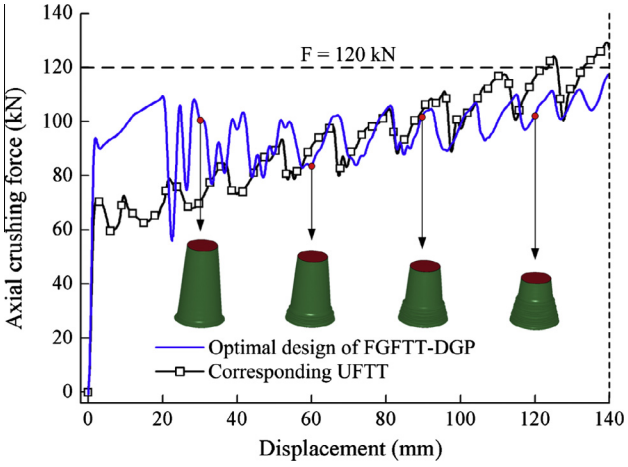

Fig. 14. Axial force–displacement curves of the optimal design of FGFTT-DGP obtained by dynamic ensemble metamodel and the corresponding UFTT.

excellent energy absorber and has a wide application prospect in vehicle engineering in future.

6. Conclusions

Functionally graded foam-filled tapered tubes (FGFTT) under axial dynamic loading have been investigated by employing finite element code LS-DYNA. The traditional uniform foam-filled tapered tubes (UFTT) with the same weight as the FGFTTs subjected to axial dynamic loading have also been investigated using LS-DYNA. The numerical results indicate that the crashworthiness of functionally graded foam-filled tapered tubes with ascending grading pattern (FGFTT-AGP) is worse than that of the corresponding UFTTs. However, the crashworthiness of functionally grade foam-filled tapered tubes with descending grading pattern (FGFTT-DGP) is generally better than that of the corresponding UFTTs. Thus, FGFTT-DGP is considered an excellent candidate of energy absorber for vehicle engineering.

In order to seek for the optimal designs of FGFTTs-DGP, the multiobjective design optimization using dynamic ensemble metamodeling method together with MOPSO algorithm have been presented. In addition, the traditional multiobjective crashworthiness design optimization with static metamodels (PRS, RBF, KRG, SVR and ensemble) has also been implemented in this study. The proposed multiobjective crashworthiness optimization method employing the dynamic ensemble metamodels actually performs better than the traditional one. The comparison of the Pareto fronts of the FGFTT-DGP and the UFTT with the same weight indicates that the crashworthiness of FGFTT-DGP is better than that of the UFTT with the same weight in most of the considered cases.

Table 6
Optimal designs of FGFTTs-DGP by using different metamodels when PCF is constrained less than 120 kN.

Metamodels	Optimal m	SEA			PCF		
		Metamodel	FEA	Error (%)	Metamodel	FEA	Error (%)
Static PRS	0.550	14.4735	15.0677	−3.9435	118.0270	117.2356	0.6751
Static RBF	0.691	15.4647	15.5062	−0.2676	119.5854	124.3151	−3.8046
Static KRG	0.591	15.3315	15.1763	1.1471	114.4921	116.8012	−1.9769
Static SVR	0.657	15.5635	15.3870	1.1471	117.7987	122.9684	−4.2041
Static ensemble	0.683	15.6234	15.4698	0.9929	119.2760	123.2085	−3.1917
Dynamic ensemble	0.560	15.1183	15.0907	0.1829	117.6285	117.5534	0.0639

Acknowledgments

This work is supported jointly by the National Natural Science Foundation of China (No. 11302075), the Specialized Research Fund for the Doctoral Program of Higher Education (20120161120009), the Open Fund of State Key Laboratory of Advanced Design and Manufacturing for Vehicle Body (No. 31275006), the Young Teacher Development Plan of Hunan University, the National Science Fund for Distinguished Young Scholars in China (No. 11225212), the National Natural Science Foundation of China (No. 11002052; 11072074), the National Science and Technology Support Program (No. 2012BAH09B02), the Specialized Research Fund for the Doctoral Program of Higher Education (20120161130001), the Science Fund of State Key Laboratory of Advanced Design and Manufacturing for Vehicle Body (No. 71275003), and the Hunan Provincial Natural Science Foundation for Creative Research Groups of China (Grant No. 12JJ7001).

References

[1] Ahmad Z, Thambiratnam DP. Application of foam-filled conical tubes in enhancing the crashworthiness performance of vehicle protective structures. Int J Crashworthiness 2009;14(4):349–63.
[2] Reid SR, Reddy TY, Gray MD. Static and dynamic axial crushing of foam-filled sheet metal tubes. Int J Mech Sci 1986;28(5):295–322.
[3] Reid SR, Reddy TY. Axial crushing of foam-filled tapered sheet metal tubes. Int J Mech Sci 1986;28(10):643–56.
[4] Reddy TY, Wall RJ. Axial compression of foam-filled thin-walled circular tubes. Int J Impact Eng 1988;7(2):151–66.
[5] Santosa SP, Wierzbicki T, Hanssen AG, Langseth M. Experimental and numerical studies of foam-filled sections. Int J Impact Eng 2000;24(5):509–34.
[6] Hanssen AG, Langseth M, Hopperstad OS. Static and dynamic crushing of circular aluminium extrusions with aluminium foam filler. Int J Impact Eng 2000;24(5):475–507.
[7] Hanssen AG, Langseth M, Hopperstad OS. Static and dynamic crushing of square aluminium extrusions with aluminium foam filler. Int J Impact Eng 2000;24(4):347–83.
[8] Seitzberger M, Rammerstorfer FG, Gradinger R, Degischer HP, Blaimschein M, Walch C. Experimental studies on the quasi-static axial crushing of steel columns filled with aluminium foam. Int J Solids Struct 2000;37(30):4125–47.
[9] Kavi H, Toksoy AK, Guden M. Predicting energy absorption in a foam-filled thin-walled aluminum tube based on experimentally determined strengthening coefficient. Mater Des 2006;27(4):263–9.
[10] Abramowicz W, Wierzbicki T. Axial crushing of foam-filled columns. Int J Mech Sci 1988;30(3/4):263–71.
[11] Wang QC, Fan ZJ, Gui LJ. Theoretical analysis for axial crushing behaviour of aluminium foam-filled hat sections. Int J Mech Sci 2007;49(4):515–21.
[12] Wang QC, Fan ZJ, Gui LJ. A theoretical analysis for the dynamic axial crushing behaviour of aluminium foam-filled hat sections. Int J Solids Struct 2006;43(7–8):2064–75.
[13] Mahmoudabadi MZ, Sadighi M. A study on the static and dynamic loading of the foam filled metal hexagonal honeycomb – theoretical and experimental. Mater Sci Eng A 2011;530:333–43.
[14] Ahmad Z, Thambiratnam DP. Crushing response of foam-filled conical tubes under quasi-static axial loading. Mater Des 2009;30(7):2393–403.
[15] Aktay L, Kröplin BH, Toksoy AK, Güden M. Finite element and coupled finite element/smooth particle hydrodynamics modeling of the quasi-static crushing of empty and foam-filled single, bitubular and constraint hexagonal- and square-packed aluminum tubes. Mater Des 2008;29(5):952–62.
[16] Mirfendereski L, Salimi M, Ziaei-Rad S. Parametric study and numerical analysis of empty and foam-filled thin-walled tubes under static and dynamic loadings. Int J Mech Sci 2008;50(6):1042–57.
[17] Meguid SA, Attia MS, Monfort A. On the crush behaviour of ultralight foam-filled structures. Mater Des 2004;25(3):183–9.
[18] Shahbeyk S, Petrinic N, Vafai A. Numerical modelling of dynamically loaded metal foam-filled square columns. Int J Impact Eng 2007;34(3):573–86.
[19] Hou SJ, Han Xu, Sun GY, Long SY, Li W, Yang XJ, et al. Multiobjective optimization for tapered circular tubes. Thin-walled Struct 2011;49(7):855–63.
[20] Song XG, Sun GY, Li GY, Gao WZ, Qing Li. Crashworthiness optimization of foam-filled tapered thin-walled structure using multiple surrogate models. Struct Multidisc Optimiz 2013;47(2):221–31.
[21] Sun GY, Li GY, Hou SJ, Zhou SW, Li W, Li Q. Crashworthiness design for functionally graded foam-filled thin-walled structures. Mater Sci Eng A 2010;527(7–8):1911–9.
[22] Yin HF, Wen GL, Hou SJ, Qing QX. Multiobjective crashworthiness optimization of functionally lateral graded foam-filled tubes. Mater Des 2013;44:414–28.
[23] Attia MS, Meguid SA, Nouraei H. Nonlinear finite element analysis of the crush behaviour of functionally graded foam-filled columns. Finite Elem Anal Des 2012;61:50–9.
[24] Zarei HR, Kröger M. Optimization of the foam-filled aluminum tubes for crush box application. Thin-Walled Struct 2008;46(2):214–21.
[25] Zarei HR, Kröger M. Crashworthiness optimization of empty and filled aluminum crash boxes. Int J Crashworth 2007;12(3):255–64.
[26] Hou SJ, Li Q, Long SY, Yang XJ, Li W. Crashworthiness design for foam filled thin-wall structures. Mater Des 2009;30(6):2024–32.
[27] Hou SJ, Han X, Sun GY, Long SY, Yang XJ, Li W, et al. Multiobjective optimization for tapered circular tubes. Thin-Walled Struct 2011;49(7):855–63.
[28] Bi J, Fang HB, Wang Q, Ren XC. Modeling and optimization of foam-filled thin-walled columns for crashworthiness designs. Finite Elem Anal Des 2010;46(9):698–709.
[29] Zhang Y, Sun GY, Li GY, Luo Z, Li Q. Optimization of foam-filled bitubal structures for crashworthiness criteria. Mater Des 2012;38:99–109.
[30] Hou SJ, Li Q, Long SY, Yang XJ, Li W. Multiobjective optimization of multi-cell sections for the crashworthiness design. Int J Impact Eng 2008;35(11):1355–67.
[31] Hou SJ, Li Q, Long SY, Yang XJ, Li W. Design optimization of regular hexagonal thin-walled columns with crashworthiness criteria. Finite Elem Anal Des 2007;43(6–7):555–65.
[32] Liu GP, Han X, Jiang C. A novel multi-objective optimization method based on an approximation model management technique. Computer Meth Appl Mech Eng 2008;197(33–40):2719–31.
[33] Jiang C, Han X, Liu GP. A sequential nonlinear interval number programming method for uncertain structures. Computer Meth Appl Mech Eng 2008;197(49-50):4250–65.
[34] Chen GD, Han X, Liu GP, Jiang C, Zhao ZH. An efficient multi-objective optimization method for black-box functions using sequential approximate technique. Appl Soft Comput 2012;12(1):14–27.
[35] Wang GG. Adaptive response surface method using inherited Latin hypercube design points. J Mech Des 2003;125(2):210–20.
[36] Goel T, Haftka RT, Shyy W, Queipo NV. Ensemble of surrogates. Struct Multidisc Optimiz 2007;33(3):199–216.
[37] Acar E, Rohani MR. Ensemble of meta-models with optimized weight factors. Struct Multidisc Optimiz 2009;37(3):279–94.
[38] Pan F, Zhu P. Design optimisation of vehicle roof structures: benefits of using multiple surrogates. Int J Crashworth 2011;16(1):85–95.
[39] Yin HF, Wen GL, Hou SJ, Chen K. Crushing analysis and multiobjective crashworthiness optimization of honeycomb-filled single and bitubular polygonal tubes. Mater Des 2011;32(8):4449–60.
[40] Kim HS. New extruded multi-cell aluminum profile for maximum crash energy absorption and weight efficiency. Thin-Walled Struct 2002;40(4):311–27.
[41] Liao XT, Li Q, Yang XJ, Li W, Zhang WG. A two-stage multi-objective optimisation of vehicle crashworthiness under frontal impact. Int J Crashworth 2008;13(3):279–88.
[42] Zhang ZH, Liu ST, Tang ZL. Crashworthiness investigation of kagome honeycomb sandwich cylindrical column under axial crushing loads. Thin-Walled Struct 2010;48(1):9–18.
[43] Santosa S, Wierzbicki T. Crash behavior of box columns filled with aluminium honeycomb or foam. Comput Struct 1998;68(4):343–67.
[44] Hallquist JO. LS-DYNA theoretical manual. California: Livemore Software Technology Corporation; 1998.
[45] Hallquist JO. LS-DYNA keyword user's manual. California: Livemore Software Technology Corporation; 2003.
[46] Zhang ZH, Liu ST, Tang ZL. Comparisons of honeycomb sandwich and foam-filled cylindrical columns. Thin-Walled Struct 2011;49(9):1071–9.
[47] Deshpande VS, Fleck NA. Isotropic constitutive models for metallic foams. J Mech Phys Solids 2000;48(6–7):1253–83.
[48] Hanssen AG, Hopperstad OS, Langseth M, Ilstad H. Validation of constitutive models applicable to aluminium foams. Int J Mech Sci 2002;44(2):359–406.
[49] Reyes A, Hopperstad OS, Berstad T, Hanssen AG, Langseth M. Constitutive modeling of aluminum foam including fracture and statistical variation of density. Eur J Mech A – Solids 2003;22(6):815–35.
[50] Crombecq K, Gorissen D, Tommasi LD, Dhaene T. A novel sequential design strategy for global surrogate modeling. In: Proceedings of the 2009 Winter Simulation Conference, Austin, TX, USA, 13–16 December 2009. p. 731–42. ISBN 978-1-4244-5770-0.
[51] Gorissen D, Couckuyt I, Demeester P, Dhaene T, Crombecq K. A surrogate modeling and adaptive sampling toolbox for computer based design. J Machine Learning Res 2010;11:2051–5.
[52] Gorissen D. Heterogeneous evolution of surrogate models. A thesis submitted for the programme master of artificial intelligence, Faculty of engineering, Catholic University of Louvain; 2007.
[53] Park JS. Optimal Latin-hypercube designs for computer experiments. J Stat Plan Infer 1994;39(1):95–111.
[54] Wang GG, Shan S. Review of metamodeling techniques in support of engineering design optimization. Int J Mech Des 2007;129(4):370–80.
[55] Erzurumlu T, Oktem H. Comparison of response surface model with neural network in determining the surface quality of moulded parts. Mater Des 2007;28(2):459–65.
[56] Forsberg J, Nilsson L. Evaluation of response surface methodologies used in crashworthiness optimization. Int J Impact Eng 2006;32(5):759–77.
[57] Hardy RL. Multiquadric equations of topography and other irregular surfaces. J Geophys Res – Atmospheres 1971;76(8):1905–15.

[58] Lophaven SN, Nielsen HB, Sondergaard J. DACE A MATLAB Kriging Toolbox. Technical report IMM-TR-2002-12, Informatics and Mathematical Modeling, Technical University of Denmark; 2002.
[59] Dellino G, Lino P, Meloni C, Rizzo A. Kriging metamodel management in the design optimization of a CNG injection system. Int J Comput Math 2009;79(8):2345–60.
[60] Clarke SM, Griebsch JH, Simpson TW. Analysis of support vector regression for approximation of complex engineering analyses. Int J Mech Des 2005;127(6):1077–87.
[61] Rajasekaran S, Gayathri S, Lee TL. Support vector regression methodology for storm surge predictions. Ocean Eng 2008;35(16):1578–87.
[62] Gunn SR. Support Vector Machines for Classification and Regression. Technical report, Image Speech and Intelligent Systems Research Group University of Southampton, UK; 1998.
[63] Liao XT, Li Q, Yang XJ, Zhang WG, Li W. Multiobjective optimization for crash safety design of vehicles using stepwise regression model. Struct Multidisc Optimiz 2008;35(6):561–9.
[64] Raquel C, Naval P. An effective use of crowding distance in multiobjective particle swarm optimization. In: Proceedings of the 2005 conference on Genetic and evolutionary computation, Washington (DC), USA; 2005. p. 257–64.
[65] Liu DS, Tan KC, Goh CK, Ho WK. A multiobjective memetic algorithm based on particle swarm optimization. IEEE Trans Syst Man Cybernetics Part B – Cybernetics 2007;37(1):42–50.